UNIVERSITY OF OKLAHOMA

GRADUATE COLLEGE

DIFFRACTION IMAGING USING GEOMETRIC-MEAN REVERSE-TIME MIGRATION AND COMMON REFLECTION SURFACE

A THESIS

SUBMITTED TO THE GRADUATE FACULTY

in partial fulfillment of the requirements for the

Degree of

MASTER OF SCIENCE

By

JIANHANG YIN
Norman, Oklahoma
2017

DIFFRACTION IMAGING USING
GEOMETRIC-MEAN REVERSE-TIME MIGRATION
AND COMMON REFLECTION SURFACE

A THESIS APPROVED FOR THE
CONOCOPHILLIPS SCHOOL OF GEOLOGY AND GEOPHYSICS

BY

Dr. Nori Nakata, Chair

Dr. Xiaowei Chen

Dr. Michael Behm

Acknowledgements

I would like to express my special appreciation and thanks to my advisor Dr. Nori Nakata. I would like to thank you for bringing me into the palace of science and teaching me how to be a good researcher. You advise on both research as well as my life have been priceless.

I would also like to thank my committee members, Dr. Xiaowei Chen and Dr. Michael Behm for serving as my committee members and their insightful comments and encouragement.

I thank everyone in our research group: Raymond Ng, Stephen Marsh, Alexandro Vera, Bailey Elizabeth Hein, Maggie Martin, Zexuan Wang, Peiyao Li, Francis Oyebanji and Sebastian Gomez Alba. I am very happy to study and work with them.

Last but not the least, I would like to thank my family: my parents, my grandparents, and my wife. They support me spiritually all the time. I love them.

Table of Contents

List of Figures

Abstract

Diffracted waves contain a great deal of valuable information about small-scale subsurface structure such as faults, pinch-outs, karsts and fractures, which are tightly related to hydrocarbon accumulation and production. Therefore, diffraction separation and imaging with high spatial resolution play an increasingly critical role in seismic exploration. In this work, we first introduce a method named geometric-mean reverse time migration (GmRTM) to image only subsurface diffractors based on the difference of the wave phenomena between diffracted and reflected waves. Numerical tests prove the advantage of this method on diffraction imaging with high resolution as well as less artifacts event if we have small number of receivers and random noise added in data. Then we propose a workflow to extract diffraction information using a full data-driven method, called common reflection surface (CRS), before we apply GmRTM. Application of this workflow shows that GmRTM further improves the quality of the image by combining with diffraction separation technique CRS in the data domain.

Chapter 1: Introduction

The seismic data contains reflection and diffraction, and most conventional seismic processing techniques aim to enhance reflection events. However, seismic response from small-size scattering objects such as faults, pinch-outs, and channels, are often shown in diffracted wavefields (Krey, 1952; Hagedoorn, 1954; Landa & Gurevich, 1998; Khaidukov, Landa, & Moser, 2004). Imaging and monitoring of these structures can be essential for the geological interpretation. On the other hand, the energy of diffraction is one or even two orders of magnitude weaker than the reflection (Klokov, Baina, Landa, Thore, & Tarrass, 2010), hence diffractions are significantly lost during the conventional seismic processing or masked in convention stacked sections. Many diffraction separation and imaging methods have been proposed to resolve this dilemma. Landa, Shtivelman, and Gelchinsky (1987) introduced a diffraction detection algorithm defined by an automatic procedure containing phase correlation of diffracted waves and application of certain statistical criteria on common-offset sections. Khaidukov et al. (2004) developed a focusing-defocusing method based on muting focused reflections at their imaginary source location and then defocusing the residual diffractions. (Fomel, Landa, & Taner, 2007) applied plane-wave destruction to separate and image diffractions. Dell and Gajewski (2011a) developed the common reflection surface (CRS) method to separate diffracted waves in the post-stack domain. This method was further modified to the pre-stack domain by Rad, Schwarz, Vanelle, and Gajewski (2014) and led to enhanced pre-stack diffrac-

tion only gathers.

One specific feature of the effect of structural discontinuities in the seismic section is associated with the presence of diffracted waves generated by the vicinity of the fault (Landa & Gurevich, 1998). The diffracted waves are considered to be generated by point sources at the location of structures, such as faults or fractures (Taner, Fomel, & Landa, 2006). Reflected waves are propagated in one direction based on the Snell's law for a specular reflector, whereas a point diffractor acts as a passive source and generates diffracted waves in multiple directions (Silvestrov, Baina, & Landa, 2016). Therefore, we modify a passive-source imaging technique for diffraction images. Among passive-source imaging techniques, such as first arrival of microseismic (Eisner, Williams-Stroud, Hill, Duncan, & Thornton, 2010), intensity imaging (Kao & Shan, 2004), and time reversal imaging (Larmat, Tromp, Liu, & Montagner, 2008), we employ geometric-mean reverse time migration (GmRTM; Nakata and Beroza (2016a, 2016b)), since GmRTM increases signal-to-noise ratio (SNR) for diffraction imaging and produces higher spatial resolution.

The energy of diffraction is very weak, and diffractions are always masked by reflections. An important step before diffraction imaging is the separation of diffractions from reflections. On the other hand, GmRTM is a method of diffraction imaging based on the pre-stack data. Therefore, we improve a pre-stack diffraction separation method based on CRS proposed by Bakhtiari Rad, Schwarz, Gajewski, and Vanelle (2017). The modified separation method uses a weighting coefficient to differentiate diffraction and reflection waves opposed to a strict criterion method.

In this work, we first suggest GmRTM formulation, and then numerically examine the performance of GmRTM on spatial resolution test and random noise suppression test. Then we introduce CRS briefly and propose a workflow for diffraction separation using CRS and diffraction imaging using GmRTM. To present the struc-

tural complexity, we furthermore apply GmRTM to the smoothed Sigsbee2A velocity model and stratigraphic Sigsbee2A velocity model after numerically diffraction separation, and compare the images obtained by GmRTM and conventional RTM. Finally, we evaluate the potential of our workflow by using stratigraphic Sigsbee2A velocity model.

Chapter 2: Methodology

2.1 GmRTM

2.1.1 Mathematical Tour

Propagation of diffracted waves from source location, $\mathbf{x}_s$, to receiver location, $\mathbf{x}_r$, through the diffractor location, $\mathbf{x}_d$, is written as:

$$D(\mathbf{x}_r, t) = \mathfrak{F}^{-1}\left\{R_{\mathbf{x}_d} S(\mathbf{x}_s, \omega) G(\mathbf{x}_r, \mathbf{x}_d, \omega) G(\mathbf{x}_d, \mathbf{x}_s, \omega)\right\}, \tag{2.1}$$

where G and S are the Green's and source functions, respectively, $R_{\mathbf{x}_d}$ is the reflection coefficient, t and ω indicate time and frequency, respectively, D is the recorded data at the location of receiver, and $\mathfrak{F}^{-1}$ is the inverse Fourier transform. The wavefield at location $\mathbf{x}$ obtained by back propagating data from each receiver $\mathbf{x}_{r_i}$ is as follows:

$$W_{r_i}(\mathbf{x}, t) = \mathfrak{F}^{-1}\left\{D(\mathbf{x}_{r_i}, \omega) \mathcal{G}^*(\mathbf{x}_{r_i}, \mathbf{x}, \omega)\right\}, \tag{2.2}$$

where * is the complex conjugate and $\mathcal{G}$ is the approximated Green's function based on a given migration velocity model. We propagate the source wavefield at the location of the active source, $\mathbf{x}_s$, in the migration velocity model and obtain the wavefield at the location $\mathbf{x}$ as follows:

$$W_s(\mathbf{x}, t) = \mathfrak{F}^{-1}\left\{S(\mathbf{x}_s, \omega) \mathcal{G}(\mathbf{x}, \mathbf{x}_s, \omega)\right\}. \tag{2.3}$$

For imaging, because W_s and W_{r_i} will pass the source location at the same time, we consider crosscorrelation of W_s and W_{r_i} at time lag equal zero for imaging condition (Claerbout, 1971). From the imaging condition of conventional RTM (Baysal, Kosloff, & Sherwood, 1983), we obtain the image I_{RTM} as follows:

$$I_{RTM}(\mathbf{x}) = \sum_t \left\{ W_s(\mathbf{x}, t) \sum_{r_i} W_{r_i}(\mathbf{x}, t) \right\}. \tag{2.4}$$

In the GmRTM, instead of summing wavefields over all receivers, we calculate the product of all receiver wavefields and then cross correlate between this product and the source wavefield at time lag equal zero (Nakata & Beroza, 2016b). The image I_{GmRTM}:

$$I_{GmRTM}(\mathbf{x}) = \sum_t \left\{ W_s(\mathbf{x}, t) \prod_{r_i} W_{r_i}(\mathbf{x}, t) \right\}. \tag{2.5}$$

This algorithm assumes that the imaging target should be considered as a secondary source. Therefore, we use equation 2.5 as the imaging condition to separate and image diffractors.

Computational cost of GmRTM is comparable to the conventional RTM since GmRTM does not need to compute Green's functions for each time interval (Nakata, Beroza, Sun, & Fomel, 2016). Furthermore we can use GmRTM for velocity estimation (Sun, Xue, Zhu, Fomel, & Nakata, 2016) as well.

2.1.2 Difference between RTM and GmRTM

We first illustrate the different behavior between diffractors and reflectors in case of GmRTM by using a schematic cartoon. Figure 2.1a shows the ray paths of diffracted waves generated by an active source at the location, $\mathbf{x}_s$. The data related to this source is represented in equation 2.1. The point diffractor emit diffracted waves in all directions when the wave from the source arrive at the location of diffractor, $\mathbf{x}_d$,

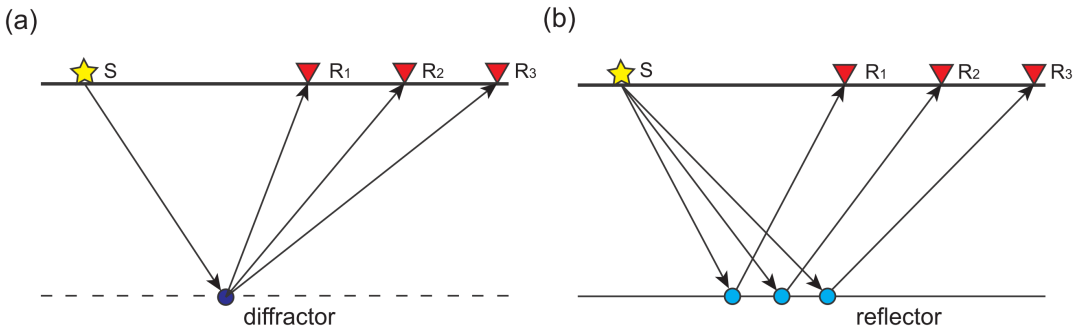

Figure 2.1: Schematic cartoon of (a) observation of diffracted waves and (b) observation of reflected waves. The black arrows indicate wave propagation, and S and R show source and receivers, respectively.

where the diffractor acts as a point source. When we apply GmRTM to image this diffractor, extrapolated source wavefield W_s and receiver wavefields W_{r_i} arrive at the location of the diffractor at the same time when the migration velocity is accurate. Based on the imaging condition shown in equation 2.5, we can obtain large values at diffractors and zero elsewhere after applying GmRTM to these wavefields.

Figure 2.1b shows ray paths for reflected waves. When the wave from the source arrive at one point on the reflector, the wavefront of reflected wave will propagate in one direction from the reflector based on Snells law. The wavefield W_{r_i} from each receiver is considered to be generated by the imaginary mirror source due to the reflectors, which pass through a common point on the reflector at different times. When we apply time reversal to the receiver wavefields in an accurate velocity model, all reversed wavefields from receivers focus at the location of the imaginary source. Thus, the product of all reversed receiver wavefields show large values at the imaginary sources location and nearly zero at the reflectors location. While in the active source imaging, the wavefield W_s generated by source has a different path from the W_{r_i}. When we apply the imaging condition of GmRTM shown in equation 2.5, the low coherence between wavefield W_s and the product of W_{r_i} result in the low value at the location of imaginary source. Therefore, we are able to suppress imaging reflected

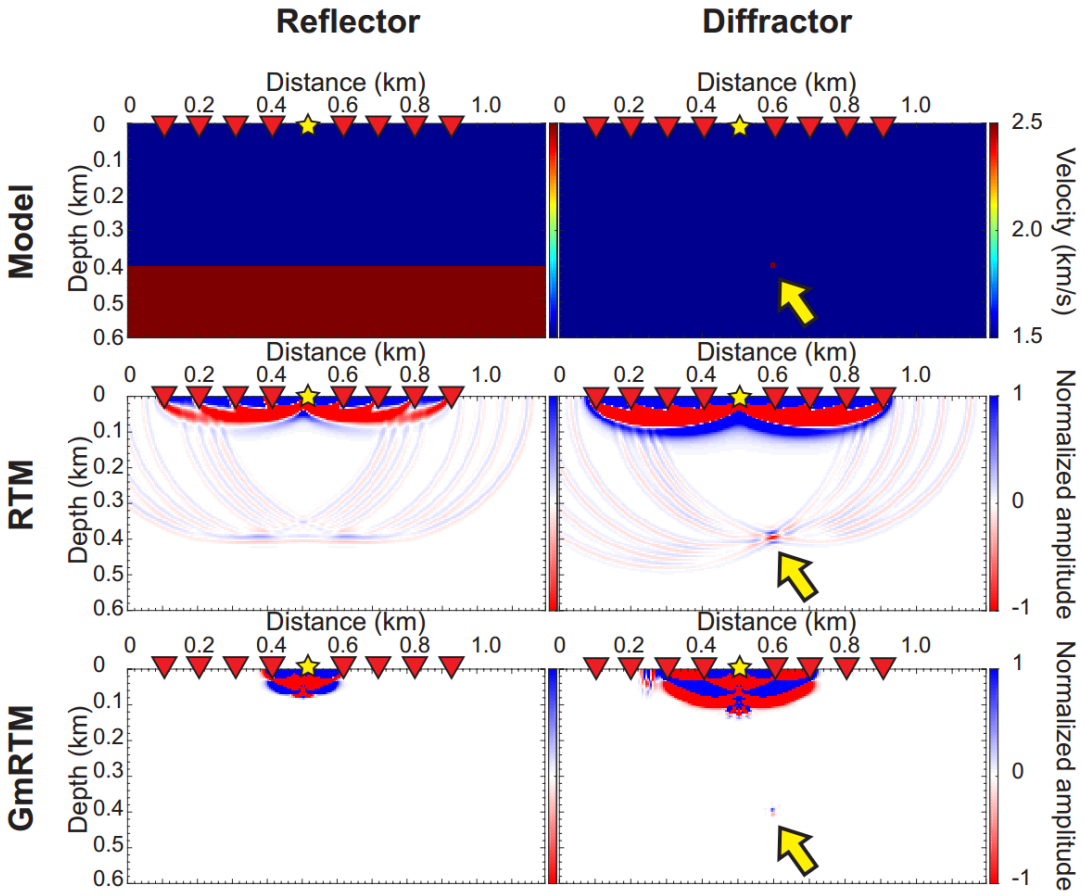

Figure 2.2: Velocity models with only one reflector at depth=0.4 km or only one diffractor at the point of (0.6, 0.4) km (top row), normalized amplitude of reflector and diffractor images obtained by RTM (middle row) and GmRTM (bottom row). The yellow star is the location of the source and red triangles indicate receivers. The yellow arrow shows the location of the diffractor.

waves and focus on diffracted waves by computing GmRTM.

Then we use 2D acoustic finite-difference numerical modeling to illustrate the different images of diffractor and reflector obtained by conventional RTM and GmRTM. In the 3D or elastic cases, we can get the same results (Nakata & Beroza, 2016a), while in this paper we only consider the 2D acoustic situation for simplicity. We use two homogeneous synthetic models with one reflector and one point diffractor at depth of 0.4 km respectively shown on the top row of Figure 2.2. The

source function we used is the Ricker wavelet with 30Hz peak frequency. The star indicates the location of the source. We use only eight receivers on the surface distributing evenly in the range of 0.1 - 0.9 km on the surface (the triangles in Figure 2.2). We don‘t consider the free surface in this synthetic model. In the reflector velocity model, we use two layers with different velocity to generate reflector. The high velocity layer with 2.5 km/s is located at the depth of 0.4 km below the low velocity layer with 1.5 km/s. The diffractor in the other model is also represented by a high velocity scatter with 2.5 km/s. We use constant density in both models. During the forward modelling, the time sampling interval is 1 ms.

First, we apply conventional RTM to these two velocity models. Because we only care about the imaging of the reflector and diffractor, we use the one layer velocity model with 1.5 km/s for migration to avoid the artifacts generated by the layered migration velocity model. In the middle row of Figure 2.2, we obtain the images of reflector and diffractor at the correct location as we expected when we apply the imaging condition of conventional RTM in equation 2.4 to the wavefields. However, eight strong artifacts of elliptical shape are present due to the limited number of receivers. According to equation 2.4, each elliptical imaging is related to a pair of wavefields from source and receiver. In other words, we actually sum all the images obtained by eight source and receiver pairs in conventional RTM. When we apply GmRTM to these two models (the bottom row of Figure 2.2), the reflector is suppressed efficiently, because when we apply the imaging condition of GmRTM to the point on the reflector the coherence among the wavefields from all receivers is relatively low, where we can get a low value in the image. For the diffractor, GmRTM creates the clearer and more focused diffractor image with much fewer artifacts. Compared with conventional RTM, we multiply all the images obtained by each pair of source and receivers instead of summing them up. This example

shows that GmRTM can not only image the much better focused diffractor but also reduced the reflector image , and we also effectively suppress artifacts similar to the passive-source imaging method as described by Nakata and Beroza (2016b).

2.1.3 Resolution

We use an acoustic homogeneous model with 12 m^2 square diffractor at the center of the model and different number of receivers to numerically address the spatial resolution of GmRTM images (Figure 2.3). The source function in this example is the Ricker wavelet with 25 Hz peak frequency. We use different number of receivers ranging from three to eleven for each test. The source and receivers are distributed evenly around a 400 m radius circle. When the source and receiver are located on the opposing sides of the target imaging zone, strong artifacts are generated by the direct waves along the ray path. Therefore, direct waves are removed prior to the application of conventional RTM and GmRTM.

In Figure 2.3, both conventional RTM and GmRTM create the image of diffractor focused at the true location when we use the correct velocity model for migration. However, in conventional RTM the small number of receivers result in elliptical artifacts related to each pair of source and receiver caused by the summation in the imaging condition. Source and receiver are located at the focus of elliptical artifact, due to the same travel distance for waves among source, imaging point and receiver. Similar artifacts are suppressed efficiently in GmRTM because of the production of wavefields in the GmRTM imaging condition, which requires the travel distances among the source, imaging point and all receivers are the same. Only the true location of diffractor matches this requirement.

On the other hand, conventional RTM blurs the diffractor images and the size of imaged diffractor does not change from seven to eleven receivers. Increasing the

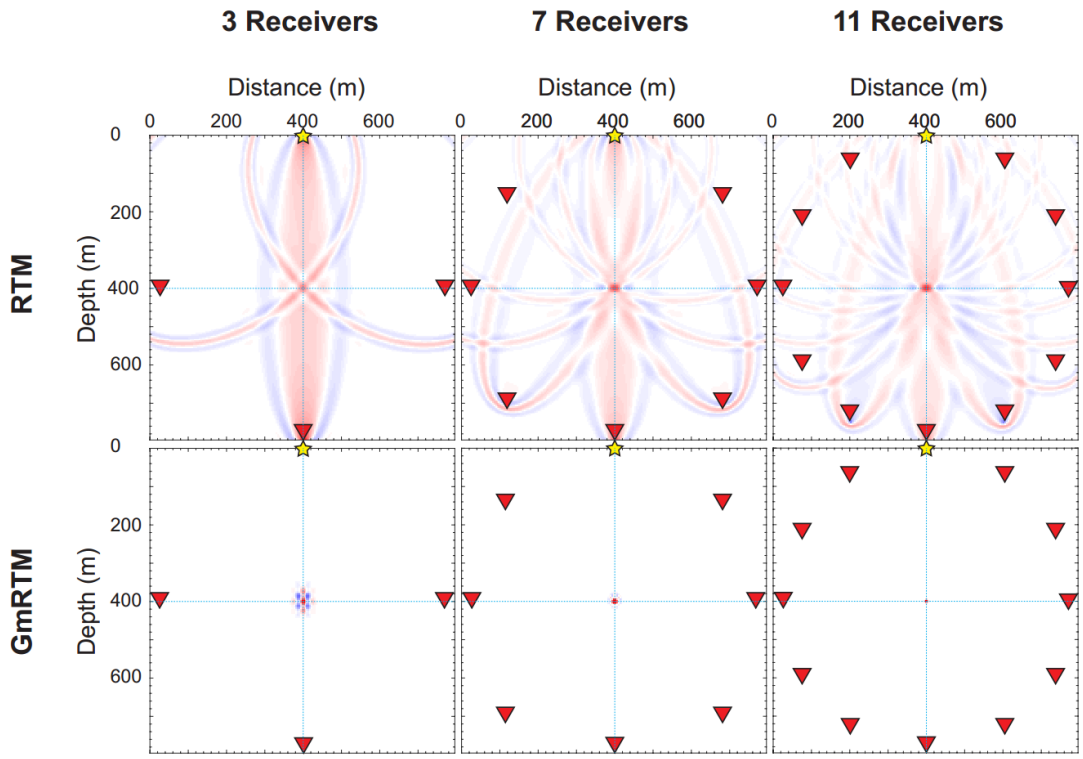

Figure 2.3: Images of a diffractor obtained by conventional RTM (top row) and Gm-RTM (bottom row) with varying number of receivers. The star and triangles indicate the location of the source and receivers, respectively. The diffractor locates at the center of the model (the intersection of the blue dashed lines).

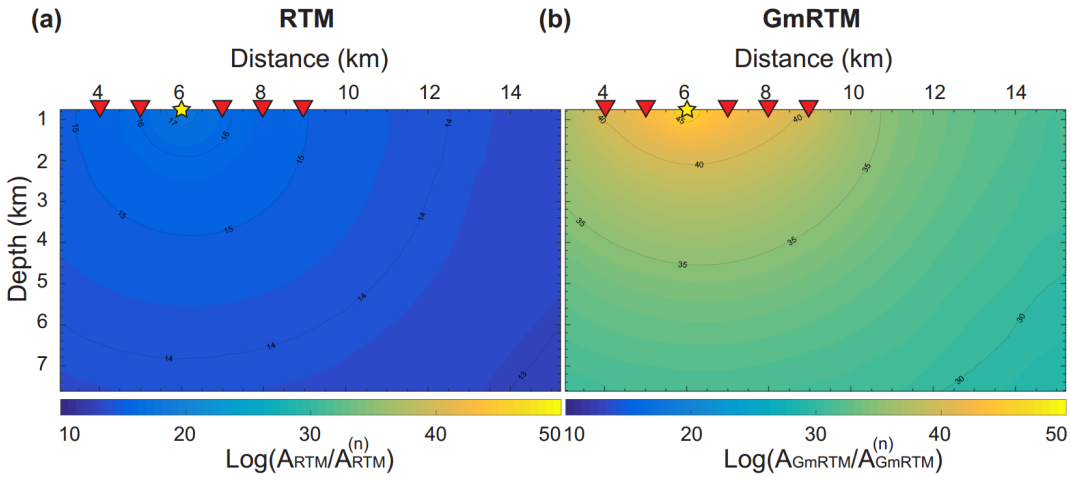

Figure 2.4: Logarithmic ratios between the amplitude of diffractor image and noise image using conventional RTM and GmRTM. The yellow star and red triangles indicate the location of the source and receivers, respectively.

number of receivers, the diffractor image obtained by GmRTM has a better focusing at the diffractor location due to the product in equation 2.5. Therefore, GmRTM can image the diffractor with a high signal noise ratio (SNR) and spatial resolution compared with conventional RTM.

2.1.4 Noise Suppression

We test the ability of GmRTM to suppress the random noise in the data. We compute the ratio of the amplitude of the image of the diffractor and root-mean square (RMS) amplitude of noise in the image using conventional RTM and GmRTM.

If we only consider the 2D loss-less media, the amplitude of data recorded by receiver from a velocity model with one diffractor at a random location is written by:

$$A_{r_i} = \frac{RA_s}{d_s d_{r_i}} \tag{2.6}$$

where A_s and A_{r_i} are the amplitude of the seismic source and data recorded by receiver r_i, respectively. R is the reflection coefficient of diffractor. d_s indicates the

distance between source and diffractor, d_{r_i} indicates the distance between receiver r_i and diffractor.

We calculate the amplitude of diffractor image (i.e. amplitude of signal) obtained by conventional RTM (A_{RTM}) and GmRTM (A_{GmRTM}) based on equation 2.4 and 2.5 as following:

$$A_{RTM} = \frac{A_s}{d_s} \sum_{i=1}^{n} \frac{A_{r_i}}{d_{r_i}} = \frac{RA_s^2}{d_s^2} \sum_{i=1}^{n} \frac{1}{d_{r_i}^2}, \tag{2.7}$$

$$A_{GmRTM} = \frac{A_s}{d_s} \prod_{i=1}^{n} \frac{A_{r_i}}{d_{r_i}} = \frac{R^n A_s^{n+1}}{d_s^{n+1}} \prod_{i=1}^{n} \frac{1}{d_{r_i}^2}, \tag{2.8}$$

here we set A_s=1 and R=1 for simplicity.

We compute the amplitude of diffractor image in a model form 3.048-15.232 km in the horizontal axis and 0.762-7.62 km in the vertical axis. The source is located at the distance of 6 km. Five receivers are used in this test, distributed along the surface from 4 km to 9 km indicated by the triangles in Figure 2.4. We assume there is only one diffractor in this model at each computation of equation 2.7 and 2.8, then we get two amplitude maps of diffrator image obtained by the imaging condition of conventional RTM and GmRTM, respectively.

Then we numerically compute the amplitude of the noise in the image domain. We inject uncorrelated white noise (0-30 Hz) at each receiver location and back-propagate them. Since the SNR in the data domain is set as 10, the RMS amplitude of noise is 0.1 (A_s=1). Then we compute summation or multiplication of the back-propagated random wavefields at each image location. Based on the imaging condition, we multiply the signal wavefield from the source with the result obtained from the previous step to map the amplitude of noise. Before computing the ratio of the amplitudes of signal and noise in the image domain, we apply a smoothing filter to the RMS noise images to remove the phase information (since we are not interested in the phase of noise). Figure 2.4 shows the ratio of the amplitudes of signal and noise

in the image domain in the logarithmic scale. We can see that the ratio obtained by GmRTM is 20-30 order of magnitude larger than conventional RTM according to the same colorbar in each figure. Therefore, GmRTM random noise suppression is much stronger than the conventional RTM and improve the SNR in the image domain.

2.2 CRS

2.2.1 Mathematical Tour

Compared with the traditional stacking, CRS stack method produces a zero offset (ZO) section by applying a CRS stacking operator to the common midpoint (CMP) data. This operator is a function of second-order Taylor approximation of the squared traveltime in the vicinity of the normal ray as a stacking trajectory (Jäger, Mann, Höcht, & Hubral, 2001)

$$t^2(x_m, h) = (t_0 + \frac{2sin\alpha}{v_0}(x_m - x_0))^2 + \frac{2t_0 cos^2\alpha}{v_0}(\frac{(x_m - x_0)^2}{R_N} + \frac{h^2}{R_{NIP}}), \quad (2.9)$$

where x_m is the midpoint near the particular midpoint (x_0), and h is the half offset, t_0 corresponds to the ZO two-way traveltime. v_0 is the near-surface velocity and the physical meaning of the three CRS parameters α, R_{NIP} and R_N are explained clearly in terms of the wavefront and ray geometries (Gelchinsky, Berkovitch, & Keydar, 1999) shown in Figure 2.5.

Compared with the conventional NMO stack, the CRS stacking operator generates a traveltime surface in the (x_m, h) domain, therefore it increases the number of traces to contribute to the subsurface imaging (Minato, Tsuji, Matsuoka, Nishizaka, & Ikeda, 2012). In addition, the CRS stack only need the near surface velocity instead of a macrovelocity model according to equation 2.9.

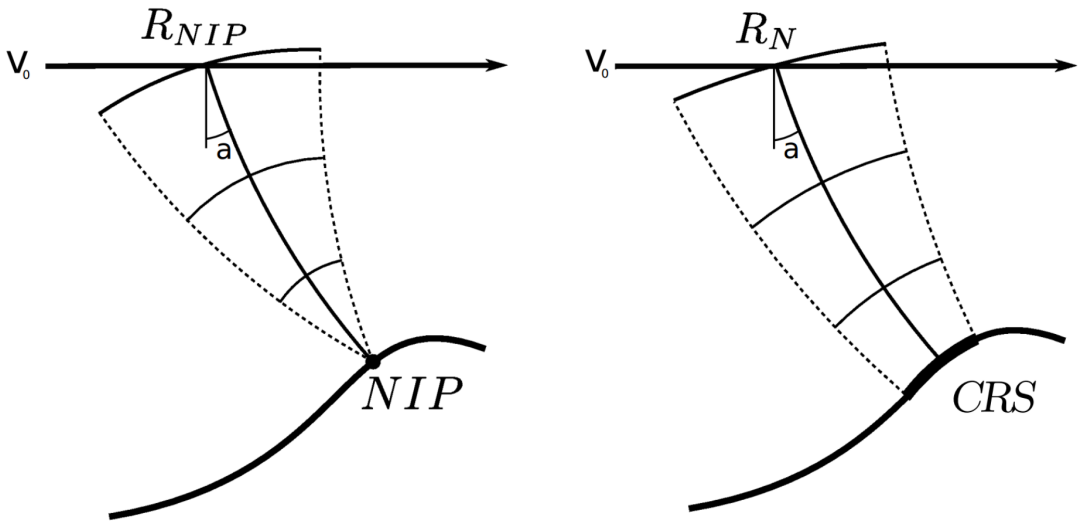

Figure 2.5: Physical meaning of CRS parameters: v_0 is the near-surface velocity and α is the incidence angle. R_{NIP} and R_N are the radius of curvature of a wavefront emitted by a point source at the normal incidence point (NIP) and normal wave generated by the reflector near NIP, respectively.

2.2.2 Coherency Analysis Measure

For each midpoint x_0 of the ZO section, the CRS stack method requires us to determine the optimum CRS parameters (α, R_{NIP}, R_N) in equation 2.9. This search is based on coherency analysis (Neidell & Taner, 1971). High coherence indicates that the recorded data is well estimated by the operator. Coherence S is defined as

$$S(\alpha, R_{NIP}, R_N; x_0, t_0) = \frac{\sum_{k(i)-\frac{w}{2}}^{k(i)+\frac{w}{2}} (\sum_{i=1}^{M} f_{i,j(i)})^2}{M \sum_{k(i)-\frac{w}{2}}^{k(i)+\frac{w}{2}} \sum_{i=1}^{M} f_{i,j(i)}^2}, \tag{2.10}$$

where $f_{i,j(i)}$ denotes the amplitude of the $j-th$ time sample in the $i-th$ of M traces. The S is calculated along the traveltime surfaces $k(i)$ of operator disposed symmetrically and parallel around the time sample i. The length of time window (w) should approximate the wavelength of the seismic source.

2.2.3 *Three-step Search Algorithm*

The three-parametric coherency-maximization problem can be divided into three 1D optimization search steps: 'automatic CMP stack', 'linear ZO stack', and 'hyperbolic ZO stack'. The automatic CMP stack is a conventional NMO stack. When we assume x_m=x_0 in equation 2.9, we obtain

$$t^2(h) = t_0^2 + \frac{2t_0 cos^2\alpha}{v_0}\frac{h^2}{R_{NIP}}, \tag{2.11}$$

which is a conventional NMO stacking operator and according to equation 2.11 we have the stacking velocity

$$V_{stack}^2 = \frac{2v_0 R_{NIP}}{t_0 cos^2\alpha}. \tag{2.12}$$

The linear ZO stack is performed in the NMO stacked section (h=0) with only linear reflectors (R_N=∞) to search for the incidence angle (α). Based on these assumptions, the CRS stacking operator can be written as

$$t(x_m) = t_0 + \frac{2sin\alpha}{v_0}(x_m - x_0). \tag{2.13}$$

In the NMO stacked section, the values of α in the range of ($-90°$, $90°$) are searched to find the value which has the highest coherency using equation 2.10. Then R_{NIP} is obtained from the values of V_{stack} and α by using equation 2.12. Finally, the hyperbolic ZO stack searches for R_N with the obtained α. When we assume h=0, the CRS stacking operator is

$$t^2(x_m, h) = (t_0 + \frac{2sin\alpha}{v_0}(x_m - x_0))^2 + \frac{2t_0 cos^2\alpha}{v_0}\frac{(x_m - x_0)^2}{R_N}. \tag{2.14}$$

For each midpoint x_0, the three CRS parameters are all obtained by finding the highest coherency in each CRS stack step, Then these parameters are used to separate diffraction from reflection in data domain.

2.2.4 Reflection Supression

In theory, the subsurface diffractors can be considered as secondary point sources, which means that R_N and R_{NIP} are equal for diffractions according to the physical meaning of the CRS parameters. While for reflectors, R_N and R_{NIP} will have very different values. Therefore we can distinguish the seismic events generated by diffractors and reflectors in the data domain. However, in reality, R_N and R_{NIP} for diffractors will not be exactly the same. So we apply the separation criterion developed by Dell and Gajewski (2011b) to identify diffraction in the data instead of using R_N=R_{NIP}:

$$T_F(x_0, t_0) = e^{-\left|\frac{R_N - R_{NIP}}{R_N + R_{NIP}}\right|}. \tag{2.15}$$

By setting a threshold of the TF value, Bakhtiari Rad et al. (2017) extracted diffracted waves and removed reflected waves in the pre-stack data domain. The value of threshold varies with the complexity of the subsurface and data quality. But diffracted waves will also be removed when the diffracted waves and reflected waves are recorded at the same time in the data. Therefore, we consider the TF value as the weighting coefficient of diffraction and reflection in order to suppress reflection and keep diffraction as much as possible instead of the criterion for diffraction separation.

Chapter 3: Numerical Example

3.1 Toy Model

We create a toy model with constant velocity, one dipping and one flat reflector and a single diffractor to investigate the performance of GmRTM and CRS method on diffraction separation and imaging (Figure 3.1). To save the computational cost of modeling, we apply Kirchhoff modeling method to obtain reflection seismic data. Then we add random noise to the data under signal-to-noise (SNR) of 10, which makes it difficult to distinguish diffraction from noise in data.

We first apply CRS method to separate diffraction in data domain. In Figure 3.2a, we obtain the incidence angle α by utilizing linear ZO stack to the NMO stacked section. We can see that for the dipping and flat reflector, the incidence angle almost doesn‘t change with the midpoint because of the physical meaning of α. While for the diffraction, the value of incidence angle changes from $-\pi$ to π. But at the location where diffraction and refection events cross each other, CRS cannot distinguish these two kinds of waves. Because the energy of reflection is much larger than that of diffraction, the α is close to zero, which is not correct for the diffraction event. Based on the α and equation 2.12, we obtain R_{NIP} of the ZO data (Figure 3.2b). Therefore, R_{NIP} meets the same problem with α on separating diffraction and reflection events when these two kinds of waves arrived at the receiver at the same time.

Then we get the R_N by applying hyperbolic ZO stack shown on Figure 3.3a. Actually, calculating CRS parameter is based on the coherency analysis, which is a kind

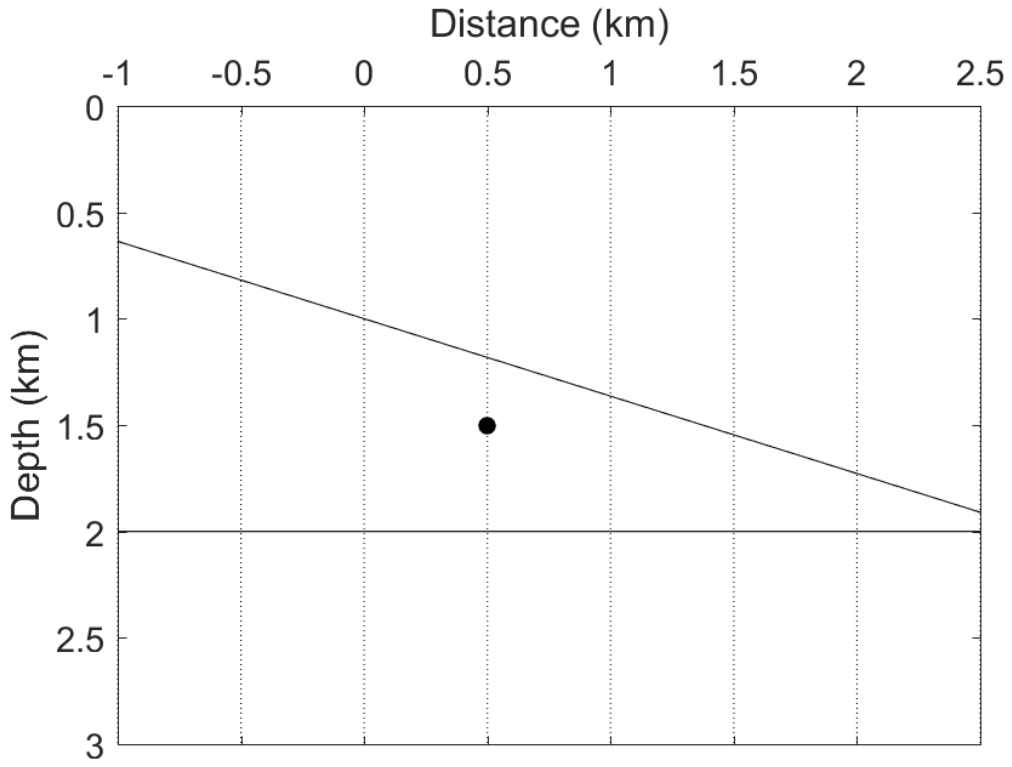

Figure 3.1: Toy model with constant velicity, cotaining one dipping and one flat reflector and a single diffractor.

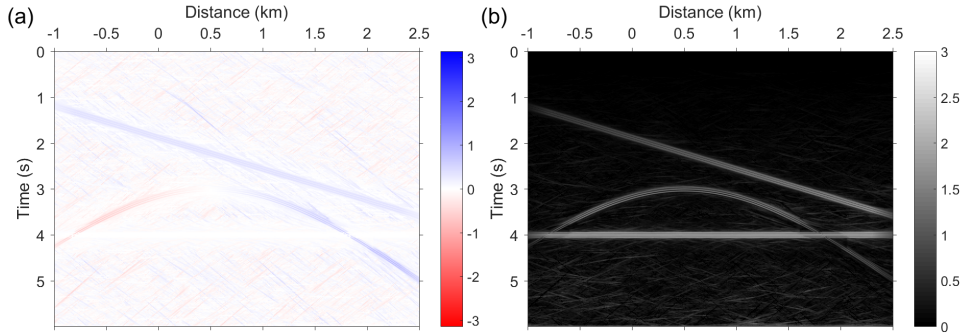

Figure 3.2: (a) The incidence angle α and (b) R_{NIP} obtained from the ZO data associated with the toy model in linear ZO stack.

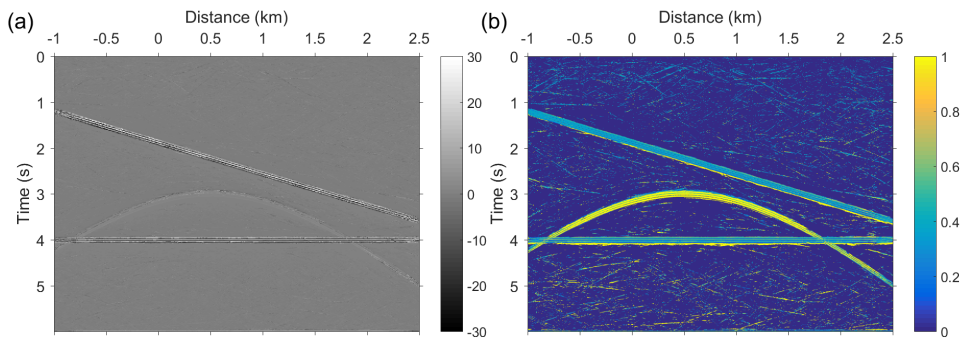

Figure 3.3: (a) R_N obtained from the ZO data associated with the toy model in hyperbolic ZO stack and (b) TF.

of image recognition method. The result of this technique is effected by the strongest component mostly in the image. Therefore, when the diffraction is covered by reflection. We cannot extract diffracted waves perfectly. We obtain TF value based on equation 2.15, we can see that the diffraction events have a larger TF compared with reflection events. While at the location crossed by reflection, TF is relatively small. Next we consider TF as the weighting coefficient of diffraction and reflection, and multiply the CMP data by TF value to suppress reflection. The ZO data before and after diffraction extraction is shown in Figure 3.4a and 3.4b, respectively. We can see that CRS can effectively suppress the random noise and reflection in the data domain. The diffraction is enhanced significantly, while at the location where diffracted wave and reflected wave cross each other, diffraction is also suppressed. This result is caused by the CRS algorithm.

Finally, we apply conventional RTM and GmRTM to the data before and after CRS diffraction separation. In Figure 3.5a, the image obtained by conventional RTM without CRS method is contaminated by the noise in the data. And the small number of receivers also generates many artifacts. It is very difficult to distinguish the diffractor in the image. Figure 3.5b shows the result of GmRTM, most of the noise is suppressed. But there are still some bright spots which are not diffrctors in the

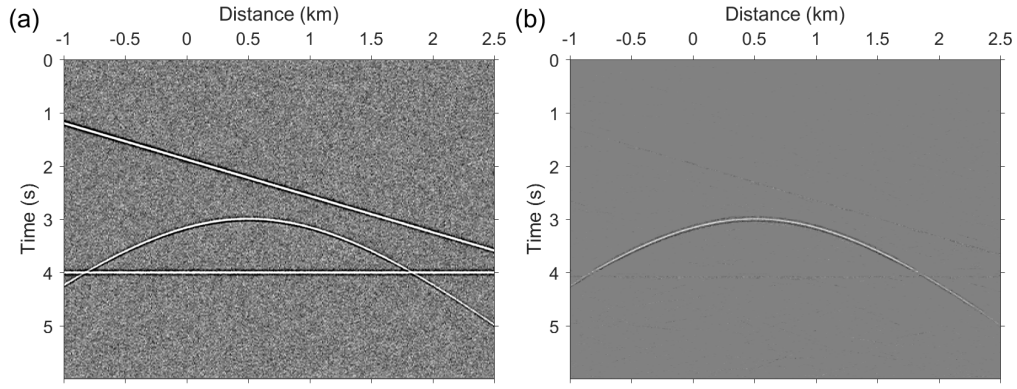

Figure 3.4: (a) ZO data associated with the toy model and (b) ZO data with only diffraction information after wavefield separation using CRS.

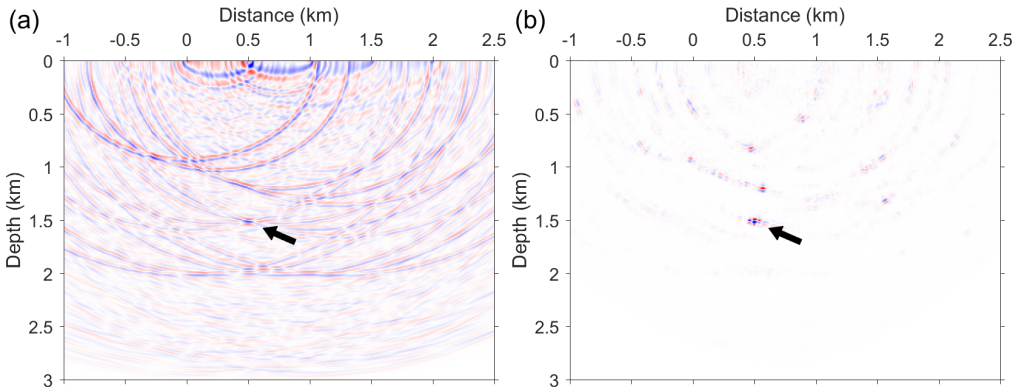

Figure 3.5: Images obtained by (a) conventional RTM and (b) GmRTM on the toy model without wavefield separation.

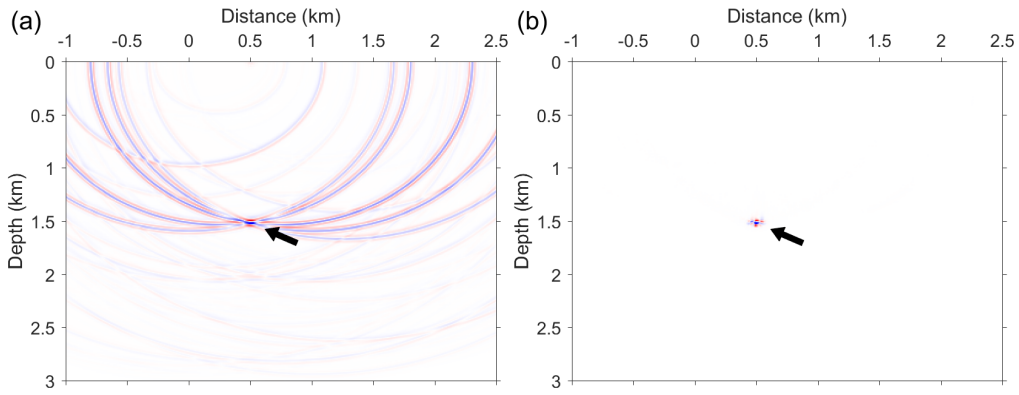

Figure 3.6: Images obtained by (a) conventional RTM and (b) GmRTM on the toy model after wavefield separation using CRS.

image.

Next we use the data after diffraction separation using CRS method to image. Figure 3.6a shows the image of diffractor obtained by the workflow of CRS and conventional RTM. Compared with the result in Figure 3.5a, the diffractor is more focused, and there are less artifacts from the random noise. But the artifacts generated by the limited number of receivers are still shown in the result. This problem is resolved by using GmRTM. In Figure 3.6b, only one clear and compact diffractor appears in the imaging result, which is much easier for interpreters to distinguish the diffractor.

This example illustrates that GmRTM is a very efficient method to image the diffractor with a high spatial resolution, it can also suppress the random noise and reflection in image domain. Combining another diffraction separation method in pre-stack domain such as CRS can improve the quality of imaging result significantly.

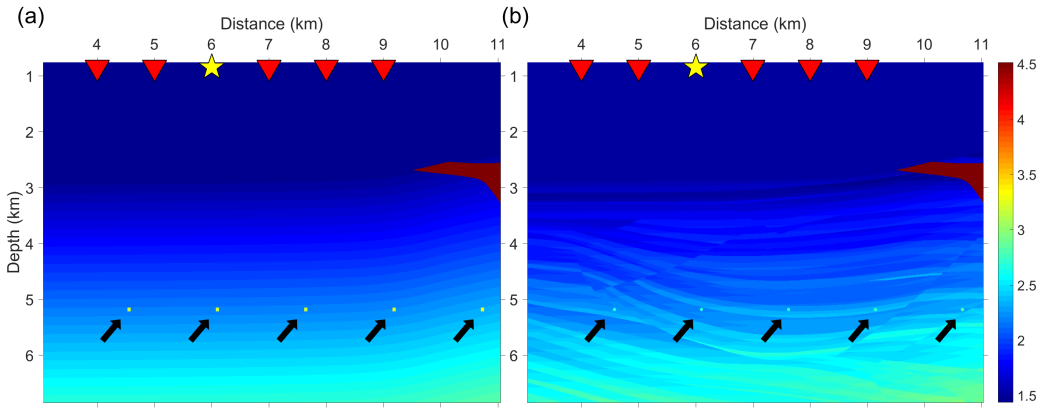

Figure 3.7: (a) A portion of Sigsbee2A smoothed velocity model with seven inserted diffractors. (b) A portion of Sigsbee2A stratigraphic velocity model. The black arrow indicate the location of diffractors.

3.2 Sigsbee2A Model

3.2.1 Smoothed Velocity Model

We use a portion of Sigsbee2A migration velocity model in Figure 3.7a to introduce some complexities into the numerical experiments but no clear reflection was obtained except the salt-body. This model is from 3.1 to 15.2 km in distance and from 0.7 to 7.6 km in depth of the migration velocity of the Sigsbee2A model without free surface (Figure 3.7a).

The image obtained by GmRTM has fewer artifacts than the image obtained by conventional RTM (Figure 3.8). In conventional RTM, image focusing and the reduction of artifacts are heavily reliant on the number of receivers for producing a significant amount of constructive wavefield interference. Reduction of artifacts is significant for diffractor imaging to avoid misinterpretation. With GmRTM, only a relatively small number of receivers is needed to achieve a clear imaging result (Figure 3.8b). GmRTM suppresses reflection images, for example the water bottom layers, as similar to Figure 2.2.

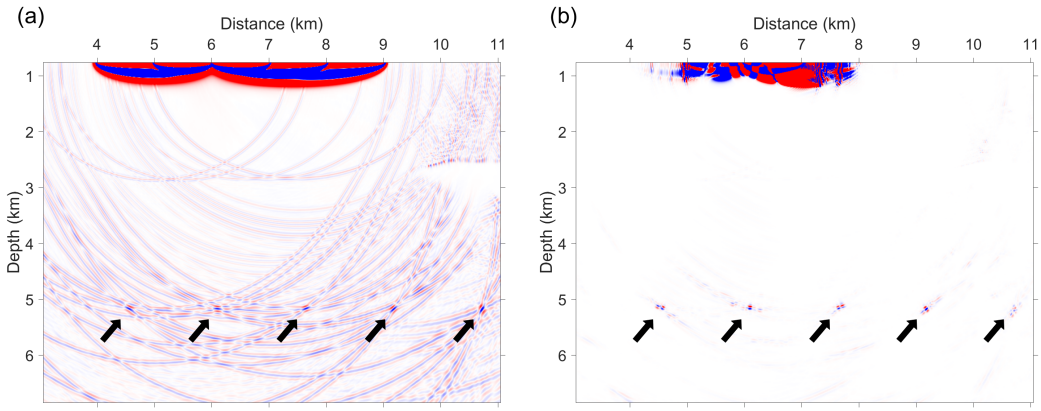

Figure 3.8: Images obtained by (a) conventional RTM and (b) GmRTM on a Sigsbee2A smoothed velcotiy model in Figure 3.7a.

For the diffractors on the right side of the velocity model, only a few waves can reach the diffractor because most of the energy from the source waves are reflected by the high-velocity salt-body. Therefore, the image amplitudes of such diffractors are weaker than the diffractors on the left side.

3.2.2 Stratified Velocity Model with Only Diffracted Waves

Next, we use a portion of the stratigraphic Sigsbee2A model (Figure 3.7b) to test the performance GmRTM after separating diffracted waves from observed data. Many diffraction separation methods have been proposed and used in field data including the Harlan transformation method (Harlan, Claerbout, & Rocca, 1984), Radon transformation method (Zhang, 2004), plane-wave destruction method (Taner et al., 2006; Fomel et al., 2007), multifocusing method (Berkovitch, Belfer, Hassin, & Landa, 2009), common surface reflection techniques (Dell & Gajewski, 2011a; Rad et al., 2014) and Mahalanobis-based method (Zhao, Peng, Du, & Li, 2016). Discussion of the separation methods is beyond the scope of this study. Here we numerically isolate diffracted waves. We first create surface records (Figure 3.9a) with the model shown in Figure 3.7b and the same model but without the diffractors. Then we subtract these

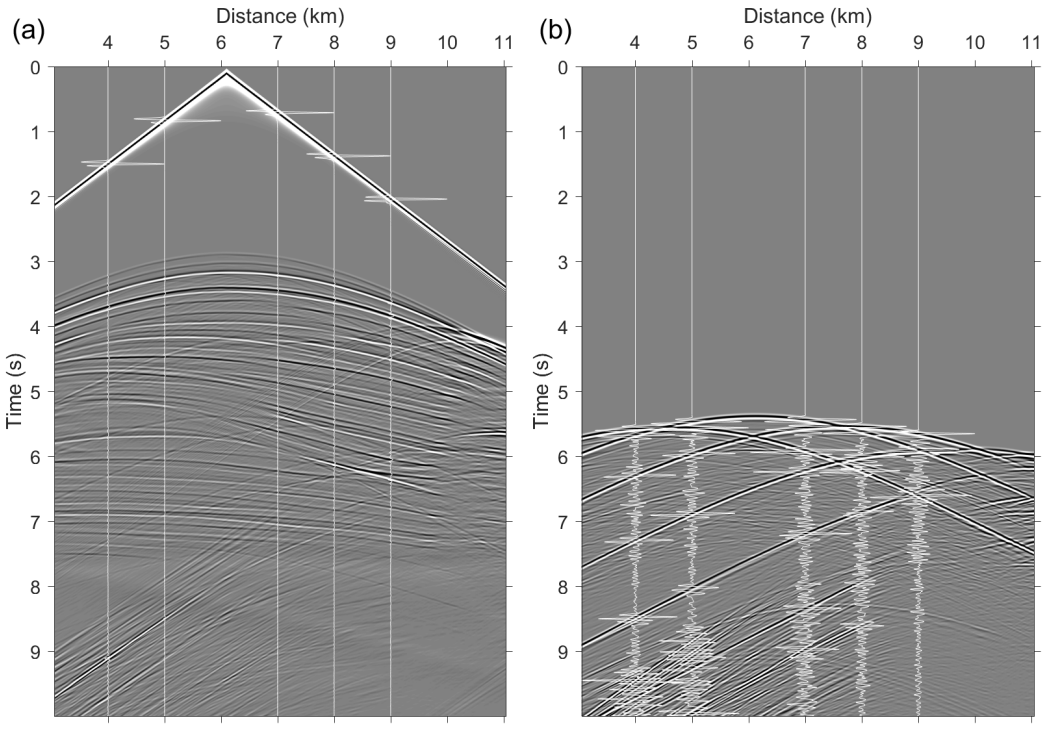

Figure 3.9: (a) Shot gather of Sigsbee2A; (b) Shot gather with only diffraction infromation of Sigsbee2A after separation. (The background image is the wavefield observed at the surface, and white vertical lines with amplitude variations indicate waveforms observed at the receivers used in migration).

records and create data which only contain waves related to the diffractors (Figure 3.9b).

After the separation, diffractors are imaged from the extracted diffracted waves using both conventional RTM and GmRTM (Figure 3.10). As similar to previous examples, GmRTM generates a sharper diffraction image compared with the conventional RTM, which is due to the multiplication in the imaging condition. The amplitude near the diffractors and everywhere else in the image is almost zero, and hence people easily identify the diffractors. GmRTM creates spatially higher resolution diffractor images and suppresses the artifacts much more strongly than conven-

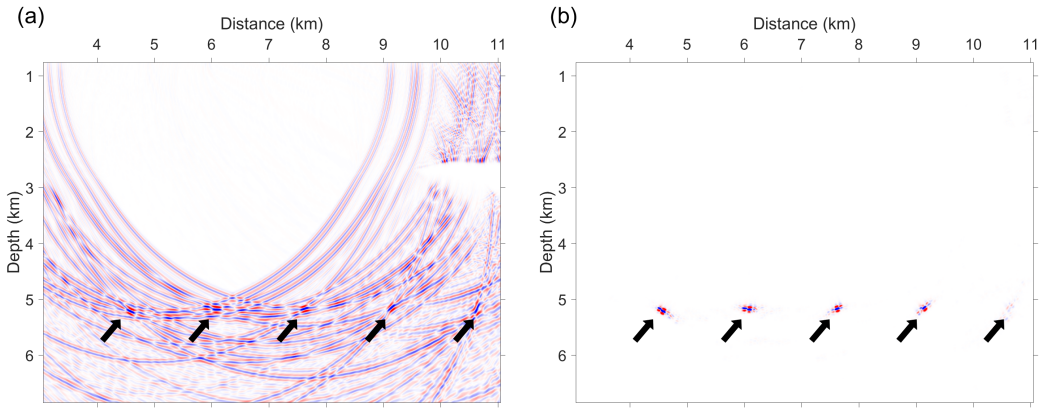

Figure 3.10: Images obtained by (a) conventional RTM and (b) GmRTM on a Sigsbee2A stratigraphic velcotiy model in Figure 3.7b after numerical wavefield separation.

tional RTM.

3.2.3 Stratified Velocity Model with CRS Separation

We illustrate the performance of CRS and GmRTM on diffraction separation and imaging using a portion of stratigraphic Sigsbee2A model with complex salt structure and six diffractors at the depth of 5.1 km (Figure 3.11).

After stacking, reflection is enhanced, and diffraction is suppressed in the zero-offset data. The part we are interested in is the diffraction. Therefore, instead of applying linear ZO stack to the post-stack data, we use the pre-stack zero-offset data to calculate the incident angle α and R_N directly (Figure 3.12).

In Figure 3.12a, the value range of α is from $-\pi$ to π. The result is obtained by calculating the optimum parameters based on the coherency analysis, which can be considered as a kind of image recognition method. Therefore, when reflected waves and diffracted waves arrive at the receiver at the same time in the zero-offset data, the algorithm cannot distinguish what kind of wave it is when the events of more than two different waves cross each other. At the location indicated by the black

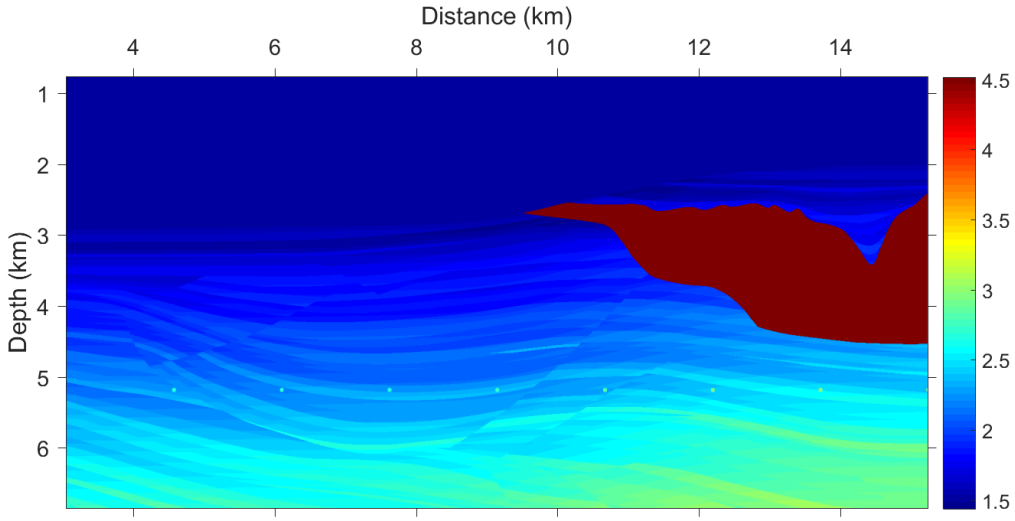

Figure 3.11: A portion of Sigsbee2A stratigraphic velocity model.

dashed rectangle box, we can see that the α value is almost zero, determined by the horizontal reflector, while it is also a part of the diffracted wave which will lead to a different α value. The R_N (Figure 3.12b) and R_{NIP} (Figure 3.13a) are both obtained from α, therefore, this result will cause the loss of diffraction information in the data domain.

Based on R_N (Figure 3.12b) and R_{NIP} (Figure 3.13a), we can obtain the TF value to identify the diffracted waves in the data as shown in Figure 3.13b. The events related to diffraction have higher TF value than the ones related to reflection. At the location indicated by the white dashed rectangle box, we get a relatively low TF value because of the limitation of image recognition. Then we multiply every seismic event in the CMP data by TF value along the trajectory at each location on the ZO data. Figure 3.14a and 3.14b show the zero-offset data before and after diffraction separation in the pre-stack data domain using the CRS method. We can see that reflection and random noise are suppressed significantly. Some of the diffraction information in the white dashed rectangle box are lost at the intersection of the diffracted wave and strong reflected wave event.

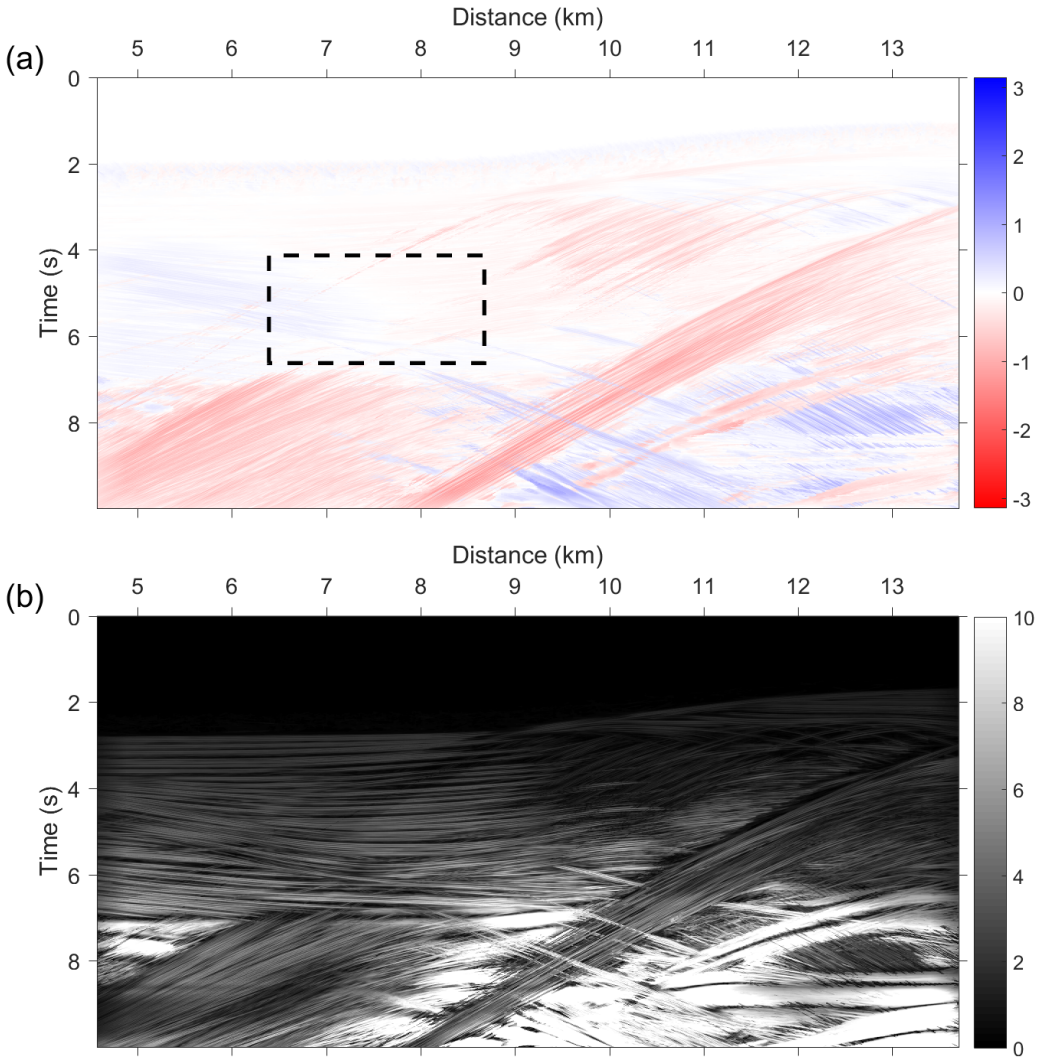

Figure 3.12: (a) The incidence angle α and (b) R_{NIP} obtained from the ZO data associated with model in Figure 3.11 in linear ZO stack.

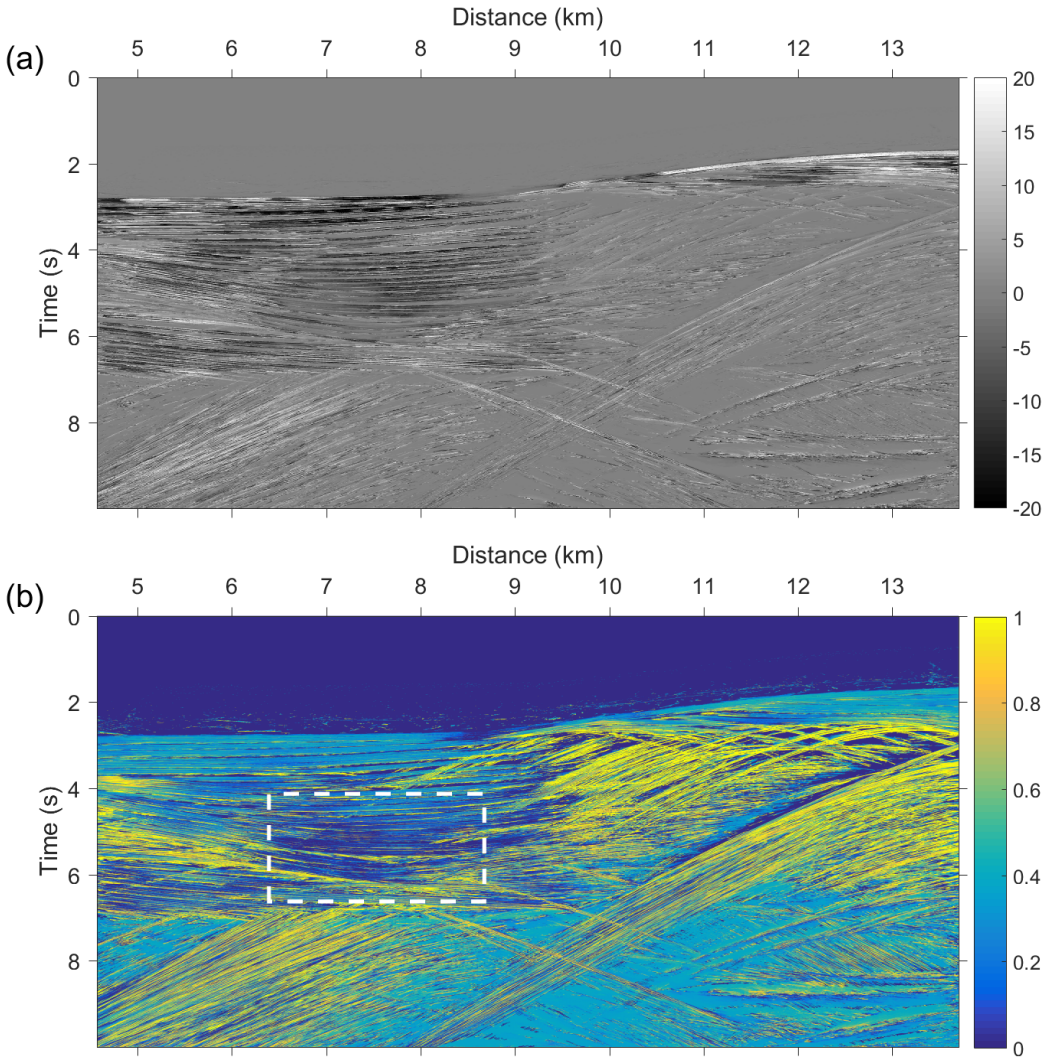

Figure 3.13: (a) R_N obtained from the ZO data associated with model in Figure 3.11 in hyperbolic ZO stack and (b) TF.

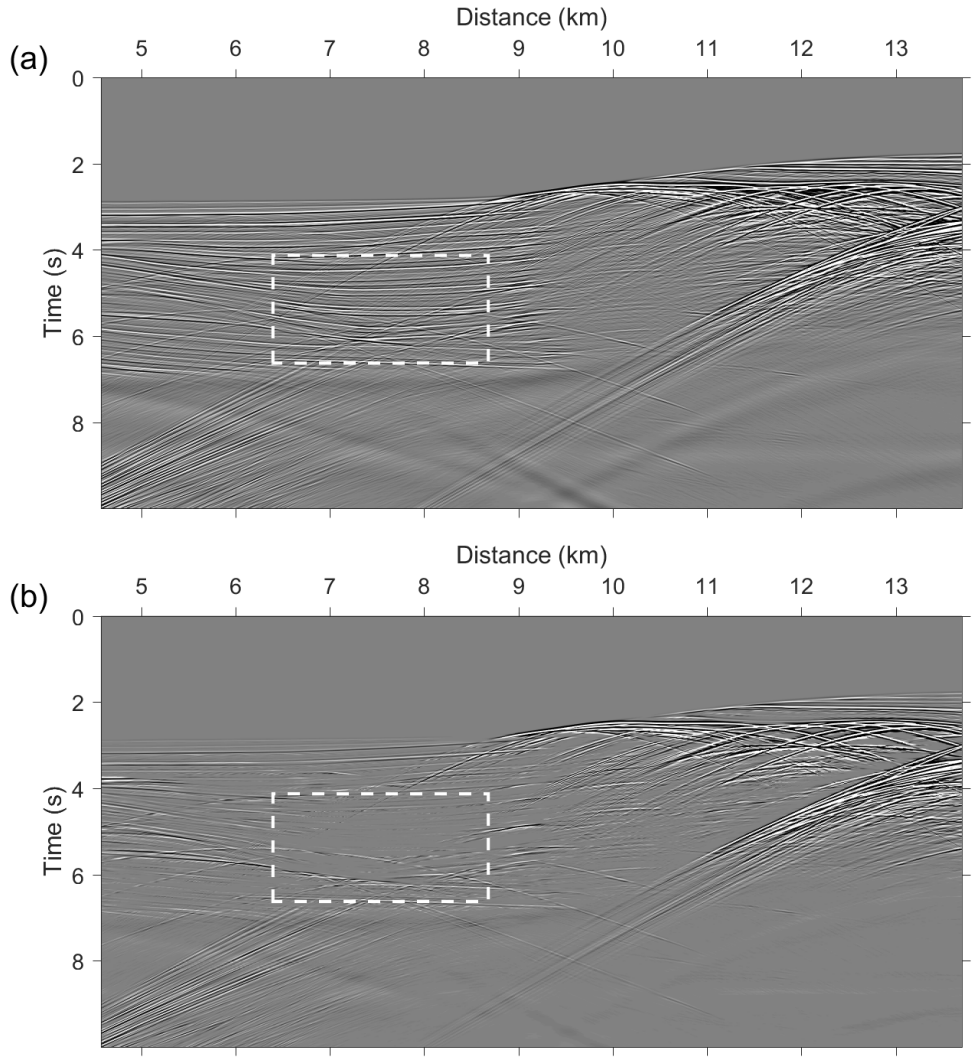

Figure 3.14: (a) ZO data associated with the Sigsbee2A model in Figure 3.11 and (b) ZO data with only diffraction information after wavefield separation using CRS.

Finally, we apply conventional RTM and GmRTM to image the diffractors in the model. For the imaging condition of GmRTM, the wavefields from each receiver and source are multiplied instead of summed together, hence the imaging result increases exponentially with the number of source and receivers. The diffraction energy value is much smaller than the reflection energy value in the data, after the imaging condition is applied, the amplitude of diffractor in the image is relatively low and it is difficult to distinguish it if there are strong reflectors around it. On the other hand, GmRTM has a stricter imaging condition, which means that it requires all the wavefields from the receivers and source to arrive at the location of diffractor at the same time. If for some reason, such as the subsurface high velocity layer, the energy of diffraction from one receiver is too weak or not recorded, we will lose the information of this diffractor using GmRTM.

Therefore, we employ the hybrid imaging condition for GmRTM to overcome this phenomena (Sun, Zhu, Fomel, & Song, 2015; Nakata & Beroza, 2016a). In order to keep the diffraction information as much as possible, we divide the receivers into four groups, and in each group the receivers distribute evenly on the surface as shown in Figure 3.15. First we sum the wavefields in each group separately to obtain four group wavefields. Then we calculate the product of the four group wavefields and stack it along the time axis to obtain the imaging result. So this is a kind of hybrid method combining conventional RTM and GmRTM.

To apply conventional RTM and GmRTM, we convert CMP data to common-shot data (Figure 3.16). In this example, the location of source is (6, 0.762) km, receivers are located on the surface from 4 km to 9km distance. By applying the revised criterion of diffraction separation, we keep most of the diffraction information and suppress the reflection. In the black dashed ellipse, some of the diffraction surrounded by the strong reflection are still suppressed. The lost diffraction information

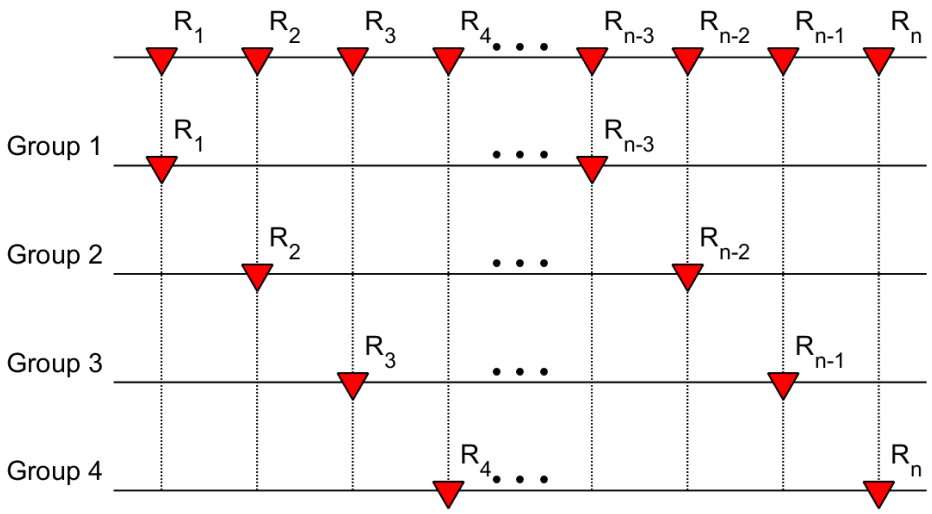

Figure 3.15: Schematic cartoon of receivers grouping. n receivers are divided into 4 groups with the same interval.

is related to the third diffractor from the left in the velocity model.

Then we first apply conventional RTM and GmRTM to the common-shot data without diffraction separation from reflection using CRS method. In Figure 3.17a, five diffractors pointed by the white arrow are imaged at the true location, and a relatively strong diffractor on the salt at the depth of 2.5 km is also shown at the correct position. Although the artifacts shown in Figure 3.8a and 3.10a are suppressed by the increasing number of receivers in the imaging result, the images of reflector still disturb the interpreters to identify the subsurface diffractors surrounded by the strong reflectors. For GmRTM, we can see that there are fewer reflectors and more focused and clear diffractors in Figure 3.17b. As we mentioned before, the seismic events related to the third diffractors from the left are covered by the events of strong reflectors indicated by the black dashed ellipse in Figure 3.16a. Therefore, the energy of the third diffractor image is relatively low. In order to keep the information of

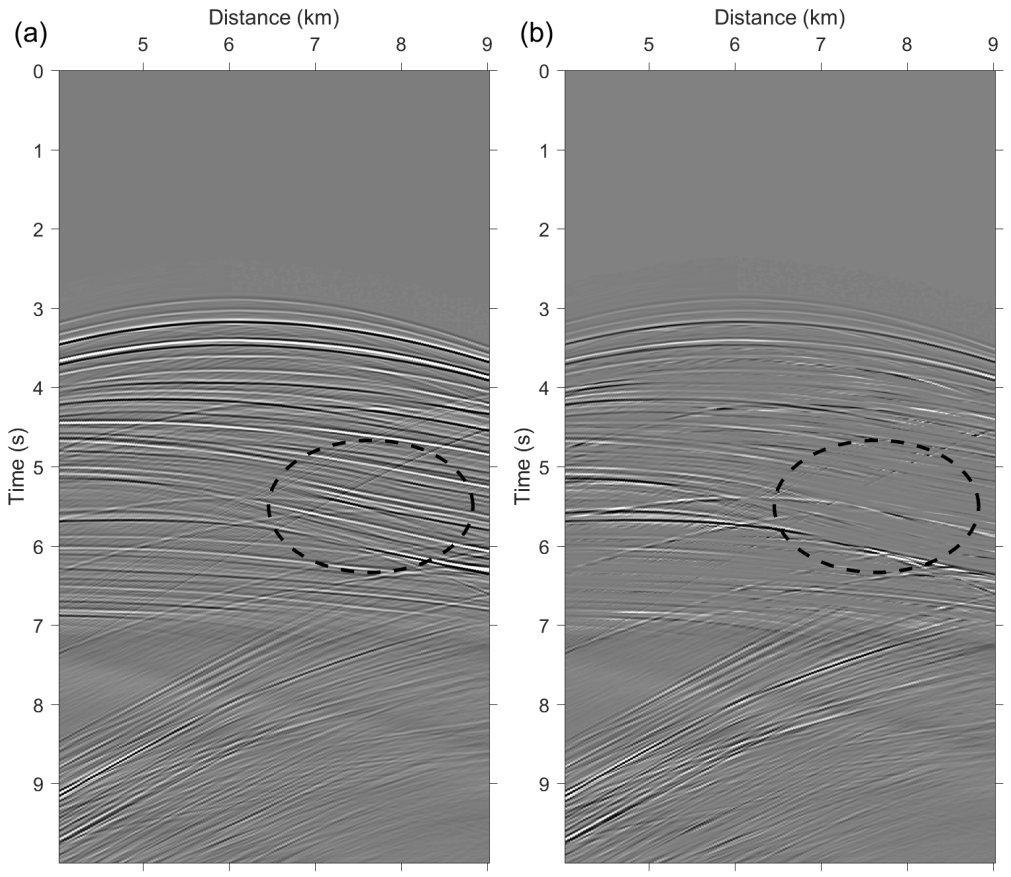

Figure 3.16: Shot gather data obtained at the location (6, 0.762) km (a) before diffraction separation in the data domain and (b) after separation using CRS.

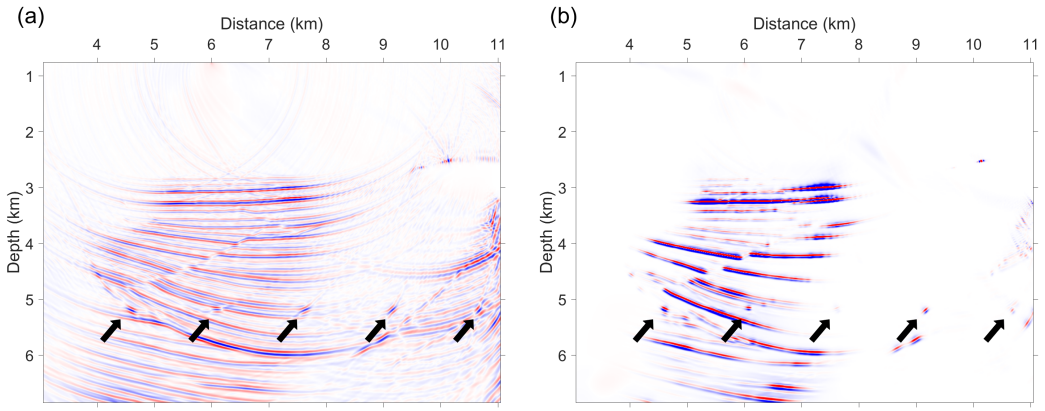

Figure 3.17: Images obtained by (a) conventional RTM and (b) Hybrid GmRTM on the stratigraphic Sigsbee velocity model without wavefield separation.

diffraction as much as possible, we bring in some reflector images by grouping the receivers before applying GmRTM. The results show that GmRTM can creates the diffractor image with high resolution and fewer reflector image and artifacts.

Next, we test the workflow we developed combining pre-stack diffraction separation method CRS with GmRTM. Figure 3.18 shows the images obtained by conventional RTM and GmRTM, respectively. In Figure 3.18a, the reflection is suppressed compared with the results shown in Figure 3.17a, which means that CRS can suppress the reflection information efficiently. However there are also many elliptic artifacts contaminating the imaging result. In Figure 3.18b, we obtain the image of the two diffractors on the left with much higher resolution and fewer artifacts and reflector image by applying GmRTM. Then we zoom in the velocity model and diffractor images at the location of two dffractors on the left side (Figure 3.19). The intersections of the black dashed lines indicate the location of the diffractors. This result confirms that the GmRTM further improves the quality of the image combining with other diffraction separation techniques.

However, in Figure 3.18b, the energy of images from the three diffractors on the right side is very weak. Due to the fact that the third diffractor from the left is

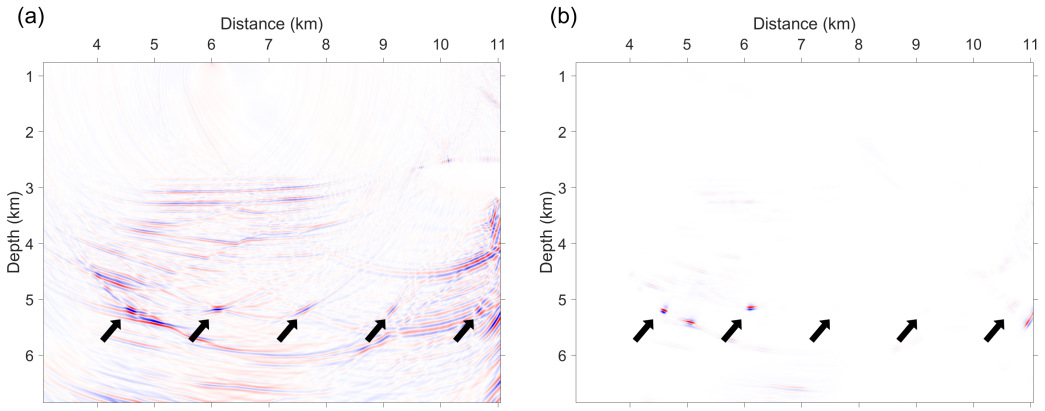

Figure 3.18: Images obtained by (a) conventional RTM and (b) Hybrid GmRTM on the stratigraphic Sigsbee velocity model after wavefield separation using CRS.

embedded in the strong reflectors and the two diffractors on right side are beneath the salt body, the energy of diffraction is suppressed during the pre-stack separation using CRS. When we decrease the scale of the colorbar, we can still visualize the diffractor image in the figure. Therefore, the performance of the pre-stack diffraction separation technique is very important to the imaging result obtained by GmRTM.

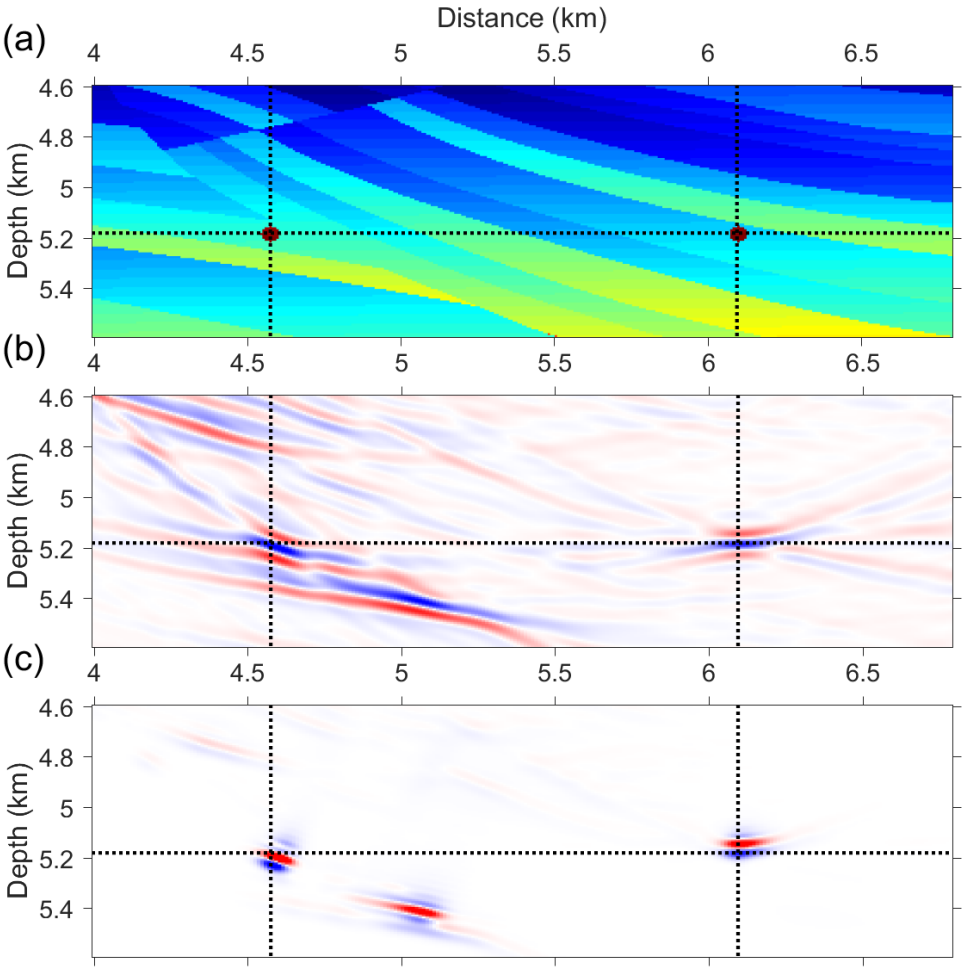

Figure 3.19: (a) Velocity model and images around the two diffractor locations on the most left side obtained by (b) conventional RTM, and (c) GmRTM. The intersections of the dashed lines in the images indicate the locations of two diffractors.

Chapter 4: Conclusions

GmRTM is effective for diffraction imaging by extracting diffraction information with higher-order crosscorrelation of receiver wavefields, creating the image with high spatial resolution, and enhancing SNR of the image. As a result of the imaging condition used, GmRTM can suppress the reflected waves and artifacts generated by the small number of receivers. The spatial-resolution test shows that GmRTM has much higher spatial resolution image compared with conventional RTM, which has a limitation by the wavelength.

With the complicated velocity structure, here we first use smoothed Sigsbee2A velocity model, GmRTM can still suppress reflectors and artifacts, and image diffractors with high spatial resolution. Then we combine GmRTM with numerical diffraction separation in the stratigraphic Sigsbee2A velocity model, the images obtained show that GmRTM further improves the quality of the image. Finally, we proposed a workflow, using the pre-stack diffraction separation method based on CRS to suppress reflection before applying GmRTM to image the diffractors. The imaging result confirms the superiority of GmRTM on diffraction imaging with high resolution and fewer reflection and artifacts. By grouping the receivers we can keep the diffraction information as much as possible. The discussion about the images in the last example shows the potential of GmRTM on diffraction imaging when a proper pre-stack diffraction separation method is applied before the application of GmRTM.

References

Bakhtiari Rad, P., Schwarz, B., Gajewski, D., & Vanelle, C. (2017). Common-reflection-surface-based prestack diffraction separation and imaging. *Geophysics*, *83*(1), 1–57.

Baysal, E., Kosloff, D. D., & Sherwood, J. W. C. (1983). Reverse time migration. *Geophysics*, *48*(11), 1514-1524.

Berkovitch, A., Belfer, I., Hassin, Y., & Landa, E. (2009). Diffraction imaging by multifocusing. *Geophysics*, *74*(6), WCA75–WCA81.

Claerbout, J. F. (1971). Toward a unified theory of reflector mapping. *Geophysics*, *36*(3), 467-481. Retrieved from http://dx.doi.org/10.1190/1.1440185 doi: 10.1190/1.1440185

Dell, S., & Gajewski, D. (2011a). Common-reflection-surface-based workflow for diffraction imaging. *Geophysics*, *76*(5), S187-S195. Retrieved from http://dx.doi.org/10.1190/geo2010-0229.1 doi: 10.1190/geo2010-0229.1

Dell, S., & Gajewski, D. (2011b). Common-reflection-surface-based workflow for diffraction imaging. *Geophysics*, *76*(5), S187–S195.

Eisner, L., Williams-Stroud, S., Hill, A., Duncan, P., & Thornton, M. (2010). Beyond the dots in the box: Microseismicity-constrained fracture models for reservoir simulation. *The Leading Edge*, *29*(3), 326–333.

Fomel, S., Landa, E., & Taner, M. T. (2007). Poststack velocity analysis by separation and imaging of seismic diffractions. *Geophysics*, *72*(6), U89-U94. Retrieved from http://dx.doi.org/10.1190/1.2781533 doi: 10.1190/1.2781533

Gelchinsky, B., Berkovitch, A., & Keydar, S. (1999). Multifocusing homeomorphic imaging: Part 1. basic concepts and formulas. *Journal of applied geophysics*, *42*(3), 229–242.

Hagedoorn, J. G. (1954). A process of seismic reflection interpretation. *Geophysical Prospecting*, *2*(2), 85–127.

Harlan, W. S., Claerbout, J. F., & Rocca, F. (1984). Signal/noise separation and velocity estimation. *Geophysics*, *49*(11), 1869–1880.

Jäger, R., Mann, J., Höcht, G., & Hubral, P. (2001). Common-reflection-surface stack: Image and attributes. *Geophysics*, *66*(1), 97–109.

Kao, H., & Shan, S.-J. (2004). The source-scanning algorithm: Mapping the distribu-

tion of seismic sources in time and space. *Geophysical Journal International*, *157*(2), 589–594.

Khaidukov, V., Landa, E., & Moser, T. (2004). Diffraction imaging by focusing-defocusing: An outlook on seismic superresolution. *Geophysics*, *69*(6), 1478-1490.

Klokov, A., Baina, R., Landa, E., Thore, P., & Tarrass, I. (2010). Diffraction imaging for fracture detection: Synthetic case study. In *Seg technical program expanded abstracts 2010* (pp. 3354–3358). Society of Exploration Geophysicists.

Krey, T. (1952). The significance of diffraction in the investigation of faults. *Geophysics*, *17*(04), 843-858.

Landa, E., & Gurevich, B. (1998). Interference pattern as a means of fault detection. *The Leading Edge*, *17*(06), 752-757.

Landa, E., Shtivelman, V., & Gelchinsky, B. (1987). A method for detection of diffracted waves on common-offset sections. *Geophys. Prosp.*, *35*(04), 359-373.

Larmat, C., Tromp, J., Liu, Q., & Montagner, J.-P. (2008). Time reversal location of glacial earthquakes. *Journal of Geophysical Research: Solid Earth*, *113*(B9).

Minato, S., Tsuji, T., Matsuoka, T., Nishizaka, N., & Ikeda, M. (2012). Global optimisation by simulated annealing for common reflection surface stacking and its application to low-fold marine data in southwest japan. *Exploration Geophysics*, *43*(2), 59–69.

Nakata, N., Beroza, G., Sun, J., & Fomel, S. (2016). Migration-based passive-source imaging for continuous data. In *Seg technical program expanded abstracts 2016* (pp. 2607–2611). Society of Exploration Geophysicists.

Nakata, N., & Beroza, G. C. (2016a, April 15). *Reverse time migration based on geometric mean for imaging seismic sources.* Google Patents. (US Patent App. 15/130,705)

Nakata, N., & Beroza, G. C. (2016b). Reverse time migration for microseismic sources using the geometric mean as an imaging condition. *Geophysics*, *81*(2), KS51-KS60. Retrieved from `http://dx.doi.org/10.1190/geo2015-0278.1` doi: 10.1190/geo2015-0278.1

Neidell, N. S., & Taner, M. T. (1971). Semblance and other coherency measures for multichannel data. *Geophysics*, *36*(3), 482–497.

Rad, P. B., Schwarz, B., Vanelle, C., & Gajewski, D. (2014). Common reflection surface (CRS) based pre-stack diffraction separation. In *Seg technical program expanded abstracts 2014* (pp. 4208–4212). Society of Exploration Geophysicists.

Silvestrov, I., Baina, R., & Landa, E. (2016). Poststack diffraction imaging using reverse-time migration. *Geophysical Prospecting*, *64*(1), 129–142. Retrieved from `http://dx.doi.org/10.1111/1365-2478.12280` doi: 10.1111/1365-2478.12280

Sun, J., Xue, Z., Zhu, T., Fomel, S., & Nakata, N. (2016). Full-waveform inversion

of passive seismic data for sources and velocities. In *Seg technical program expanded abstracts 2016* (pp. 1405–1410). Society of Exploration Geophysicists.

Sun, J., Zhu, T., Fomel, S., & Song, W.-Z. (2015). Investigating the possibility of locating microseismic sources using distributed sensor networks. In *Seg technical program expanded abstracts 2015* (pp. 2485–2490). Society of Exploration Geophysicists.

Taner, M. T., Fomel, S., & Landa, E. (2006). Separation and imaging of seismic diffractions using plane-wave decomposition. In *Seg technical program expanded abstracts 2006* (pp. 2401–2405). Society of Exploration Geophysicists.

Zhang, R. (2004). Imaging the earth using seismic diffractions. *CDSST annual report*.

Zhao, J., Peng, S., Du, W., & Li, X. (2016). Diffraction imaging method by mahalanobis-based amplitude damping. *Geophysics*, *81*(6), S399–S408.